

Silicon heterojunction back-contact solar cells by laser patterning

<https://doi.org/10.1038/s41586-024-08110-8>

Received: 20 March 2024

Accepted: 25 September 2024

Published online: 1 October 2024

 Check for updates

Hua Wu^{1,7}, Feng Ye^{1,7}, Miao Yang¹, Fei Luo¹, Xiyan Tang¹, Qing Tang¹, Haoran Qiu¹, Zhipeng Huang¹, Genshun Wang^{1,2}, Zhaoqing Sun^{1,3}, Hao Lin², Junzhe Wei¹, Yunpeng Li¹, Xiaoqiang Tian¹, Jinsheng Zhang¹, Lei Xie¹, Xiaoyu Deng¹, Tuan Yuan¹, Mingzhe Yu¹, Yong Liu¹, Ping Li¹, Hao Chen¹, Shenghou Zhou^{1,3}, Qishu Xu¹, Peng Li¹, Jun Duan¹, Jiansheng Chen¹, Chunxiu Li¹, Shi Yin¹, Bo Liu¹, Chang Sun¹, Qiao Su^{1,2}, Yichun Wang⁴, Hao Deng⁴, Tian Xie⁴, Pingqi Gao², Qian Kang³, Yongzhe Zhang³, Hui Yan³, Ningyi Yuan⁵, Fuguo Peng¹, Yunlai Yuan^{1,6}, Xiaoning Ru¹, Bo He¹, Lan Chen¹, Jianbo Wang¹, Junxiong Lu¹, Minghao Qu¹, Chaowei Xue¹, Jianning Ding⁶, Liang Fang¹, Zhenguo Li¹ & Xixiang Xu¹

Back-contact silicon solar cells, valued for their aesthetic appeal because they have no grid lines on the sunny side, find applications in buildings, vehicles and aircraft and enable self-power generation without compromising appearance^{1–3}. Patterning techniques arrange contacts on the shaded side of the silicon wafer, which offers benefits for light incidence as well. However, the patterning process complicates production and results in power loss. We employed lasers to streamline the fabrication of back-contact solar cells and enhance the power-conversion efficiency. Using this approach, we produced a silicon solar cell that exceeded 27% efficiency. Hydrogenated amorphous silicon layers were deposited onto the wafer for surface passivation and to collect light-generated carriers. A dense passivating contact, which differs from conventional technology practice, was developed. Pulsed picosecond lasers operating at different wavelengths were used to create the back-contact patterns. The approach developed is a streamlined process for producing high-performance back-contact silicon solar cells, with a total effective processing time of about one-third that of the emerging mainstream technology. To meet the terawatt demand, we developed indium-less cells at 26.5% efficiency and precious silver-free cells at 26.2% efficiency. Thus, the integration of solar solutions into buildings and transportation is poised to expand with these technological advances.

Silicon solar cells usually have a single electrode on each side so that they are front- and back-contact cells. The electrode grid on the sunny side obstructs light, thus reducing energy input. Placing both terminals on the shaded side creates back-contact solar cells that are potentially more efficient and also aesthetically appealing. In 1975, Schwartz and Lammert at Purdue University introduced interdigitated-back-contact solar cells⁴. Swanson at Stanford University later developed a similar point-contact solar cell, achieving a record efficiency of 22.3% in 1988⁵. SunPower, established in 1985, has since become a pioneer in commercializing interdigitated-back-contact technology. The heterojunction back-contact (HBC) cell structure was first developed by Lu et al. at the University of Delaware in 2007⁶. Subsequently, companies like Sharp, Panasonic and Kaneka have improved HBC technology^{7,8}. In 2017, Kaneka achieved a record 26.7% power-conversion efficiency (PCE) for Si solar cells with the HBC structure⁹. This record was later surpassed by LONGi with a 26.8% Si heterojunction (SHJ) front- and back-contact

solar cell in 2022¹⁰. These achievements are guiding efforts in improving Si solar cell performance through combining the heterojunction technology with the back-contact structure. A big challenge in making HBC solar cells is the patterning on the back side, which usually introduces process complexity and power output losses. Although potential solutions have been explored, such as photolithography, inkjet printing, *in situ* shadow masking and laser patterning, they face technological or cost issues that are still inadequately addressed in mass production^{11–16}. Laser patterning is considered the most economical method for fabricating back-contact solar cells; however, the highest PCE of fully laser-processed HBCs reported so far by the Interuniversity Microelectronics Centre is only 22.5%¹³. Another challenge is how to decouple the use of rare indium and precious silver from the heterojunction technology, which is crucial as we enter the terawatt era. In this work, we propose a solution to these challenges in manufacturing high-efficiency HBC solar cells for a sustainable future.

¹Central R&D Institute, LONGi Green Energy Technology Co. Ltd, Xian, China. ²School of Materials, Institute for Solar Energy Systems, Sun Yat-sen University, Guangzhou, China. ³Beijing Key Lab of Microstructure and Properties of Solids, Faculty of Materials and Manufacturing, Beijing University of Technology, Beijing, China. ⁴Wafer Business Unit, LONGi Green Energy Technology Co. Ltd, Xian, China. ⁵Jiangsu Collaborative Innovation Centre for Photovoltaic Science and Engineering, Changzhou University, Changzhou, P. R. China. ⁶Institute of Technology for Carbon Neutralization, Yangzhou University, Yangzhou, P. R. China. ⁷These authors contributed equally: Hua Wu, Feng Ye. e-mail: xuechaowei@longi.com; dingjn@yzu.edu.cn; fangliang4@longi.com; lzg@longi.com; xuxixiang@longi.com

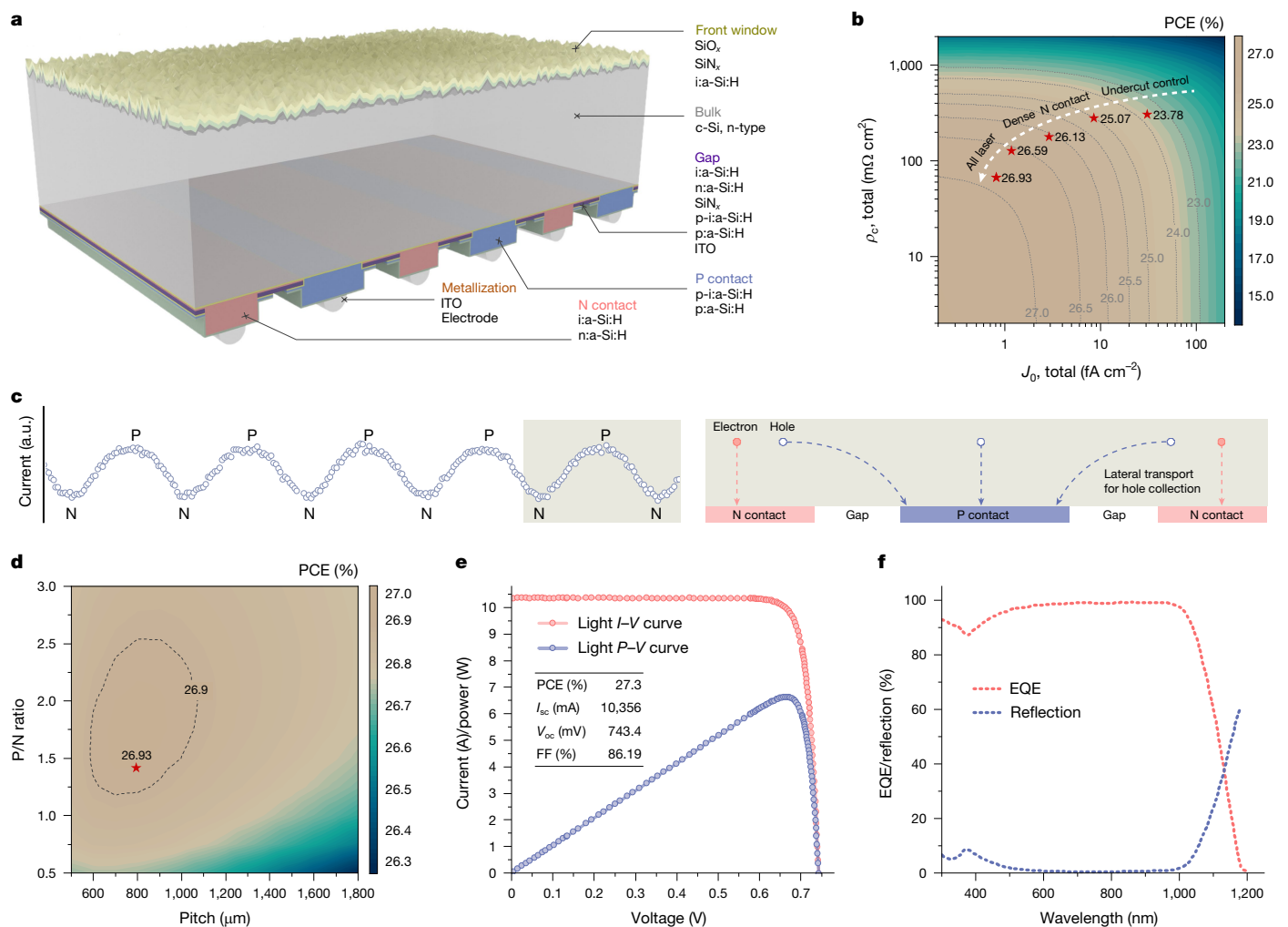


Fig. 1 | HBC solar cell development. **a**, State-of-the-art HBC solar cell configuration; fabrication process flow shown in Extended Data Fig. 1. **b**, Simulation of efficiency as a function of contact resistivity (ρ_c) and recombination current density (J_0). **c**, Electrical shading. The current induced by a light beam was measured across six pitches. Less current was collected at N contacts compared to P contacts due to lateral hole transport loss. The red N's and blue P's mark the periodic positions of N and P contacts, respectively. A schematic of the loss mechanism in one pitch is also shown. **d**, Simulation of

efficiency as a function of the P/N ratio and pitch. The red pentagram marks the optimal combination of the P/N ratio and pitch for the record cells. **e**, Current-voltage (I - V) and power-voltage (P - V) curves of the record cell certified by the Calibration and Test Center of the Institute for Solar Energy Research in Hamelin. **f**, External quantum efficiency (EQE; measured at the Calibration and Test Center) and reflection (measured in-house) for the record cell. a.u., arbitrary unit; J_{sc} , short-circuit current; FF, fill factor.

HBC solar cell design

In this section, we outline the practical structure of an HBC solar cell and identify key properties for achieving Si solar cells that surpass 27% PCE (Fig. 1a). At the device level, processes aiming to reduce the recombination current density (J_0) and contact resistivity (ρ_c) contribute to the overall PCE (Fig. 1b)¹⁷. SHJ uses thin hydrogen-containing Si layers as passivating contacts. The N-contact typically comprises intrinsic/n-type amorphous layers (i:a-Si:H/n:a-Si:H), whereas the P-contact comprises intrinsic/p-type amorphous layers (p:i:a-Si:H/p:a-Si:H). We use 'i' for the intrinsic amorphous silicon layer in the N-contact and 'p-i' for the P-contact in the rest of this article, unless otherwise specified. The back pattern of our cells has about 70,000 mm of borders. Thus, besides the surface passivation, this unique feature of back-contact cells makes it crucial to minimize the recombination at the borders. With these factors in mind, we identified three key process advances for achieving better than 27% PCE: dense passivating contacts, laser patterning without laser-beam-induced damage and undercut control through refining the wet chemical process (Fig. 1b).

Another important factor when making back-contact solar cells is electrical shading¹⁸ (Fig. 1c). Besides reducing the bulk and surface recombination, this loss can be reduced by optimizing the contact pitch and carefully choosing the resistivity of the substrate. The 780 μm pitch (P-contact/gap/N-contact/gap) and P/N ratio of 1.4 (P-contact width over N-contact width) used in our cell processes were based on simulation results (Fig. 1d). Our simulations comprehensively considered their impact on the effects of shading (short-circuit current density J_{sc}) and on the overall carrier recombination and transport (the fill factor and the open-circuit voltage V_{oc}). The most efficient cells were on 175- μm -thick (after texturing) 1.3–1.8 Ωcm silicon wafers.

On a full M6 wafer (total area 274.4 cm^2), the highest PCE of 26.93% was achieved with low J_0 (0.8 fA cm^{-2}) and ρ_c ($\rho_{c,n} = 25$ and $\rho_{c,p} = 40 \text{ m}\Omega \text{cm}^2$ for the N-contact and P-contact resistivities, respectively) values, and $J_{sc} = 42.10 \text{ mA cm}^{-2}$. Masking the wafer edge, a PCE of 27.3% was attained at a designated area of 243.0 cm^2 (Fig. 1e). The external quantum efficiency and reflection measured for this cell are shown in Fig. 1f. The lower current density of the full-area solar cell was attributed to imperfect passivation at the wafer edges, which indicates that potential improvements could be made by ameliorating the edge losses.

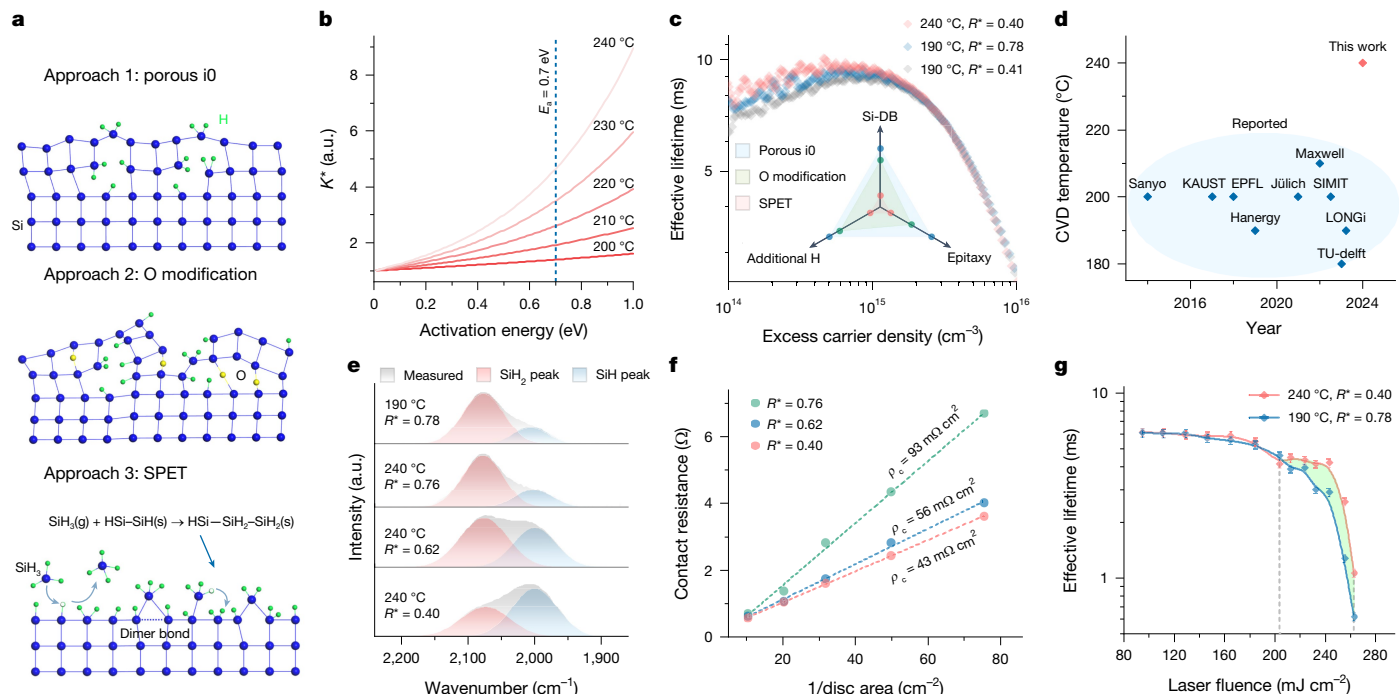


Fig. 2 | Dense passivating N contact for HBC. **a**, Three approaches for suppressing epitaxy growth. **b**, Relation between the relative reaction rate coefficient K^* and activation energy at different temperatures. The blue line indicates the activation energy of the Si–Si dimer at the lower limit. **c**, Effective lifetimes of wafers passivated by different i0 layers. Inset, Radar chart qualitatively comparing the passivation by different i0 layers. **d**, Summary of CVD temperatures used by the principal teams as reported in the literature and

used by this work^{9,10,19,40–45}. **e**, Fourier transform infrared spectroscopy profiles of i0 layers prepared at 190 °C and 240 °C with different microstructure factors. Gaussian curves were fitted to the SiH_2 and SiH peaks. **f**, Linear fits of the contact resistivity calculated using the Cox and Strack method (Extended Data Fig. 1). In **c–f**, i1 was always tuned to have the same R^* as i0. **g**, Effective lifetime of i0/i1/i2 stack passivation for different i0 layers versus laser fluence. SPET, SiH_2 promotion at elevated temperature.

Advanced passivating contact for HBC

A rear-positioned N contact obviates the need for oxygen incorporation or crystallization to reduce parasitic light absorption. In previous studies, we uncovered two approaches for epitaxy suppression in i:a-Si:H layer deposition to achieve enhanced passivation (Fig. 2a)^{19,20}. A sandwiched passivation layer (i0/i1/i2) with an H-rich porous first layer (i0) deposited onto an oxygen-modified c-Si surface offered an optimal solution. However, this H-rich layer is less conductive compared to a denser state. We use the word ‘dense’ in this work to describe layers containing less hydrogen (having a low microstructure factor R^*). We developed dense passivating contacts to address both passivation and contact resistivity for N contacts.

After being dipped in HF, the c-Si surface became H-covered with Si dangling bonds (Si-DBs) and strained Si–Si dimers. As the main constituent of the silane plasma, SiH_3 radicals can possibly: (A) become adsorbed on Si-DBs to form SiH–SiH_2 , (B) become adsorbed on dimers to form $\text{Si–SiH}_2\text{–SiH}$ or (C) abstract H atoms from the Si surface, returning to the SiH_4 gas phase^{21–23}. With forward reactions A and B proceeding, the newly formed SiH_2^- sites adsorbed more SiH_3 energetically, impeding adatom diffusion for epitaxy through a layer-by-layer mode^{24–26}. However, when the rates of both the A and B reactions are low, what probably happens is that nanotwins form through an island growth mode and degrade surface passivation²⁷. This can largely be prevented by elevating the temperature, courtesy of the much higher activation energy of reaction B (0.7–0.9 eV) compared to A (nearly zero) and C (0.02 eV)^{21,27}. This is illustrated in Fig. 2b. The ratio of the reaction rates at temperatures over 190 °C to that at 190 °C (K^*) increased rapidly with the activation energy. An elevated temperature will also accelerate the release of H, rendering the film denser and, thus, more conductive²⁸. Besides the density of Si-DB and the epitaxy, another factor impacting the i:a-Si:H/c-Si interface passivation is the extra H

supplied from overlying layers (Fig. 2c, inset). If Si-DBs and epitaxy are suppressed, the requirement of H supply from the i1 reservoir will also be alleviated.

With this SiH_2 promotion at elevated temperature approach, excellent passivation was achieved using an i0 layer deposited at 240 °C. A higher effective lifetime, especially at lower to mid-injection levels, was exhibited compared to the layers deposited at lower temperatures (Fig. 2c). Notably, 240 °C is a significant divergence from the common practice that favours 180–210 °C for heterojunctions (Fig. 2d). The excellent passivation quality in combination with the relatively low hydrogen content of 18% (Fig. 2e) indicates that Si-DBs and epitaxy at the interface were, indeed, suppressed, which confirms that the adoption of a denser i1 layer did not compromise the passivation, as aforementioned. In the results shown in Fig. 2c–f, i1 was always tuned to have the same R^* as i0. Tuning R^* for both i0 and i1 from 0.76 to 0.40 resulted in a drastic drop in ρ_c from 93 to 43 $\text{m}\Omega \text{ cm}^2$ (Fig. 2f and Extended Data Fig. 2). Note that these ρ_c values and effective lifetimes were measured after the high-intensity illuminated annealing (Extended Data Fig. 3a,b). We also found that a denser i1 layer was more resistant to laser fluence (Fig. 2g). More detailed properties and deposition parameters for i0, i1 and i2 can be found in Extended Data Table 1.

Laser patterning

Highly precise and rapid laser systems offer substantial benefits in the high-volume photovoltaic (PV) industry. A single gigawatt-scale production line can handle approximately 15,000 wafers per hour, equivalent to one-third of the capacity of the entire semiconductor industry²⁹. At present, a definitive pathway for laser-patterned HBC solar cells with efficiencies beyond 26% is not available due to laser-beam-induced damage, which specifically causes V_{oc} and fill factor loss by degrading the amorphous passivating contact or the c-Si interface^{30,31}. The highest

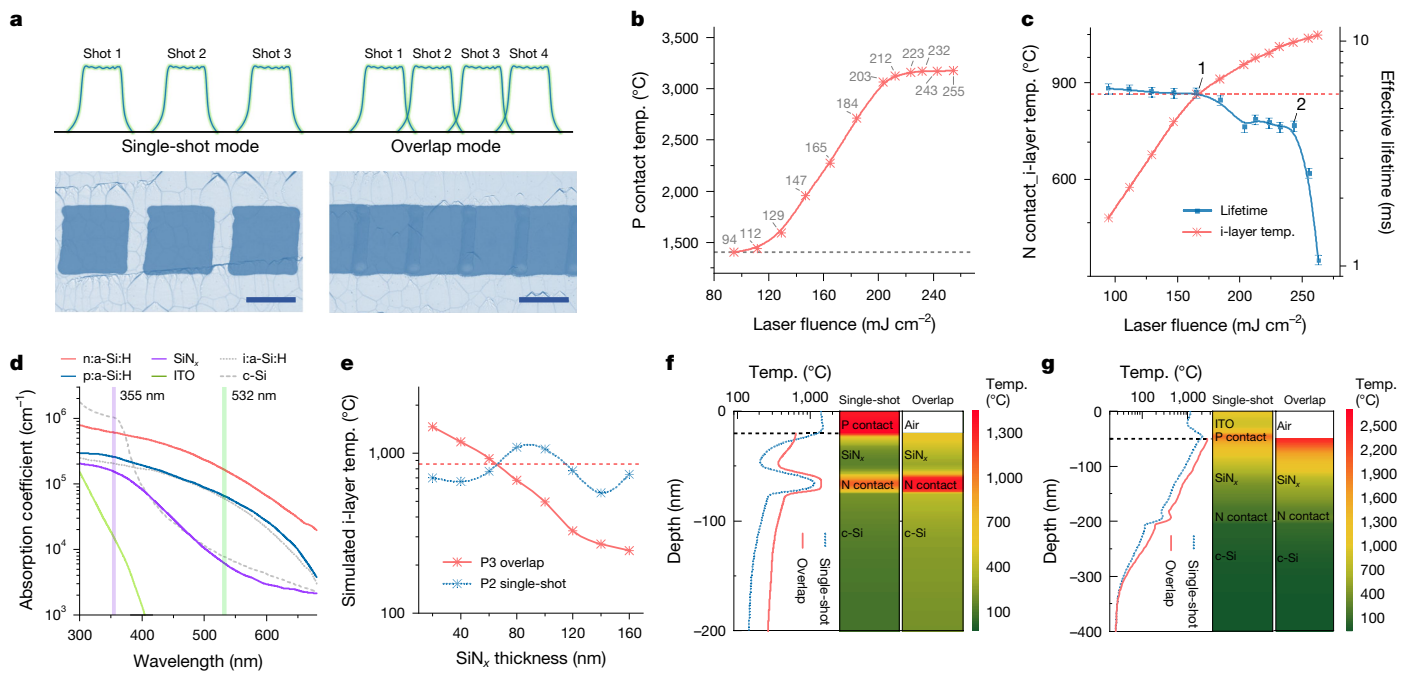


Fig. 3 | Laser patterning. **a**, Operating mode of the laser beam: single-shot versus overlap. The height of a laser shot profile represents the energy intensity across the spot. The laser spots were examined under an optical microscope. **b**, Simulated P-contact temperature versus laser fluence. **c**, Comparison of N-contact passivation quality, as indicated by the effective lifetime at $5 \times 10^{15} \text{ cm}^{-3}$ and by the simulated i-layer temperature. Points 1 and 2 indicate the first and second turning points on the effective lifetime curve.

reported efficiency for laser-patterned HBC is only 22.5%, significantly lower than the 26.7% efficiency achieved with photolithography.

In our fabrication of HBC solar cells, three laser-patterning steps (P1, P2 and P3) were used to create the interdigitated N/P polarity by selectively removing N-contact, P-contact and indium tin oxide (ITO) layers, respectively (Extended Data Fig. 1). The top-hat-shaped laser beam was operated in two modes. Overlap mode, used in P1 and P3, completely removed a layer, whereas the single-shot mode used in P2 preserved the region between consecutive shots (Fig. 3a). The single-shot mode created partial, instead of full-area, contact between the n:a-Si:H film and the ITO layer. We found that this was necessary to maintain the passivation of the underlying N contact. For the same purpose, pulsed green (532 nm) and ultraviolet (355 nm) picosecond lasers were used in P2 and P3, respectively, to minimize heat impact³².

The relations among the laser fluence, the passivation quality of i:a-Si:H/n:a-Si:H and the SiN_x thickness was explored through simulation and experiments. Taking the P2 process, for example, the temperatures of both the P-contact (Fig. 3b) and the N-contact i layer (Fig. 3c) were simulated with COMSOL Multiphysics by coupling the two-temperature model with the wave optics module. The optical properties of the layers required in the simulation were measured (Fig. 3d). Based on the simulation results, we determined that a threshold laser fluence of 94 mJ cm⁻² was required to open the P-contact (Extended Data Fig. 4a). Starting from this threshold, an increasing sequence of laser fluences was applied (Extended Data Fig. 4b), and the corresponding effective lifetimes were measured (Fig. 3c). An appropriate laser fluence should be high enough to effectively remove the P-contact and, in combination with subsequent wet chemical processes, prepare a clean interface for the contact with ITO, yet it should not be high enough to damage the N-contact passivation. In practice, the annotated point 1 in Fig. 3c was employed in P2. The simulated i-layer temperature offers more insights into the degradation mechanism of the N-contact passivation. The two annotated inflection points on the effective lifetime curve at

d, In-house measured absorption coefficients for i:a-Si:H, n:a-Si:H, p:a-Si:H, SiN_x ($n = 2.5$) and ITO layers compared with c-Si as a reference. **e**, Simulation of i-layer temperature during P2 and P3 versus SiN_x thickness. **f**, Temperature distribution within the stacked layers following P2 laser fluence. **g**, Temperature distribution within the stacked layers following P3 laser fluence. Scale bars, 100 μm . temp., temperature.

165 and 243 mJ cm⁻² laser fluences correspond to 860 and 1,060 °C, respectively. In this regard, the passivation degradation in the initial stage was probably due to hydrogen debonding under heat impact. At temperatures close to 1,000 °C, structural changes in the i layer can occur, leading to a continuous decline in the effective lifetime. Beyond point 2, the passivation was completely compromised.

The SiN_x thickness was determined from both the P2 and P3 processes. The simulated i-layer temperature in P2 increased at certain SiN_x thicknesses due to interference (Fig. 3e). However, in P3 the i-layer temperature monotonically decreased with increasing SiN_x thickness due to strong absorption by the SiN_x layer at 355 nm. A thickness of around 140 nm was deemed to be suitable, as the temperature of the i layer could be kept below 700 °C in both processes. The simulated temperature profiles with 140 nm SiN_x during a picosecond laser pulse in P2 and P3 are illustrated to provide an intuitive understanding (Fig. 3f,g).

Notably, devices fabricated with full laser patterning outperformed those using photolithography for P3 (Extended Data Fig. 4c-f). This can probably be attributed to the damage to the front i:a-Si:H passivation caused by the alkaline media used to remove the photoresist. We consistently observed a higher J_{sc} and fill factor in fully laser-processed HBC solar cells. Note that completely removing the entire photoresist without leaving a noticeable residue is challenging and potentially requires the application of chemicals suitable for the semiconductor industry but not for the PV industry.

Undercut control

A primary issue at the pattern borders is undercutting, which complicates the passivation of the c-Si surface beneath the SiN_x mask formed during the wet chemical process following the P1 step. The P1 process ablates the mask i layer (a sacrificial amorphous silicon layer used for P1 patterning) in the p region to expose the SiN_x film, which is then etched away by an HF solution. This is followed by a KOH etch with two

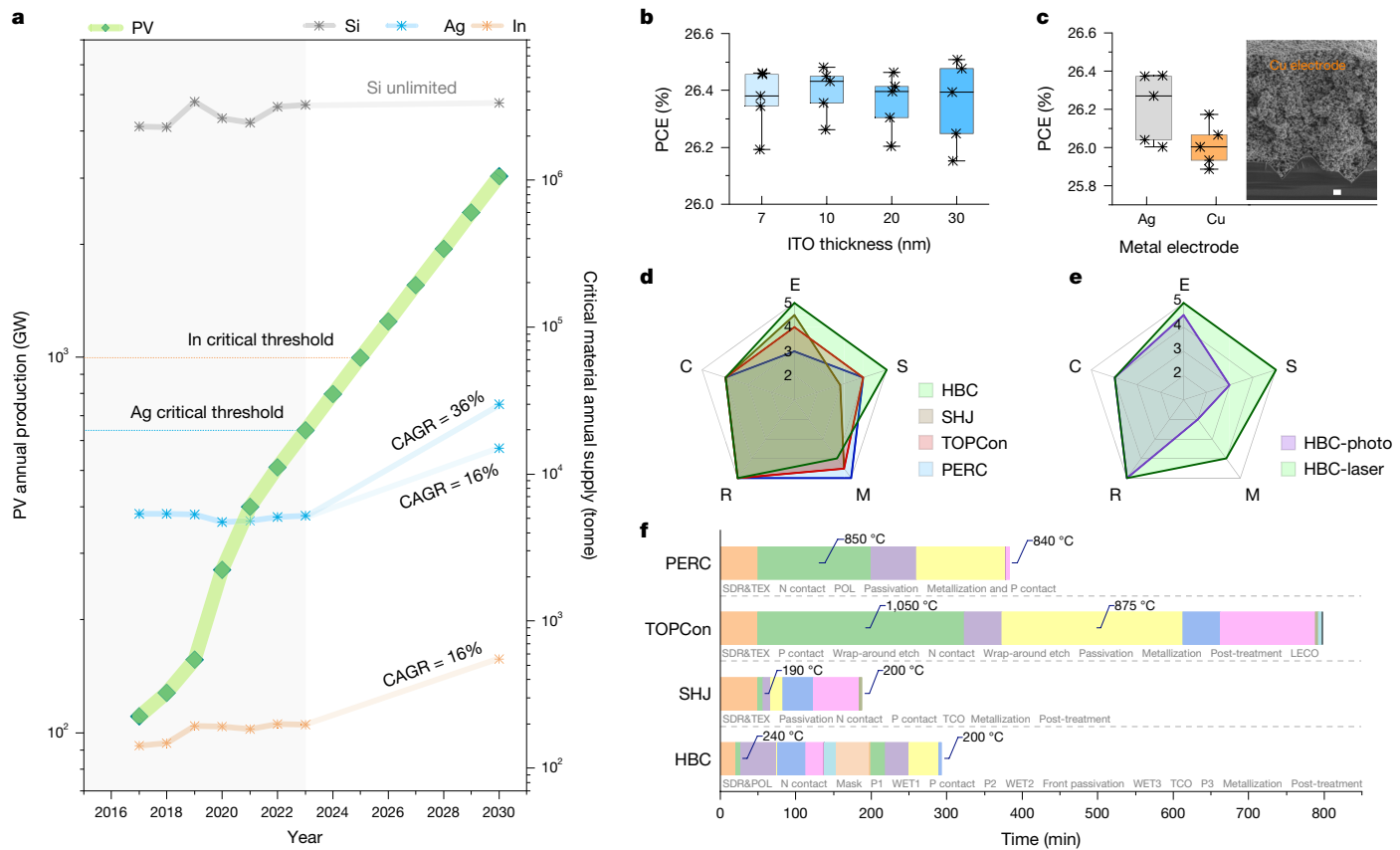


Fig. 4 | Terawatt-scale sustainability analysis. **a**, PV annual production and critical material annual supply. **b**, Efficiency of HBC solar cells with different ITO thicknesses. **c**, Efficiency of HBC solar cells metallized by an Ag electrode or a Cu electrode. Inset, scanning electron microscopy image displaying the cross-sectional morphology of the Cu electrode. **d**, ESMRC chart for HBC, SHJ, TOPCon and PERC. **e**, ESMRC chart for HBC patterned by photolithography for P3 (HBC-Photo) or laser P3 (HBC-Laser). **f**, Processing times for PERC, TOPCon, SHJ and HBC.

SHJ and HBC. The highest-temperature steps in the processes are labelled. In **b** and **c**, the top lines, bottom lines, lines in the box and boxes represent maximum values, minimum values, median values and 25–75% distributions, respectively. Scale bar, 1 μ m. E, efficiency; S, scalability; M, manufacturability; R, reliability; C, circularity; LECO, laser-enhanced contact optimization; POL, polishing; SDR&POL, saw damage removal and polishing; SDR&TEX, saw damage removal and texturing.

objectives: (1) to remove any remaining mask in other regions and (2) to eliminate the exposed i:a-Si/n:a-Si in the p region so as to prepare a fresh surface for P-contact deposition. An over-etch is typically performed to ensure the latter goal is achieved. During this process, the masked i:a-Si/n:a-Si in adjacent regions is etched laterally, whereas the SiN_x remains largely unaffected (Extended Data Fig. 5a,b). The protruding SiN_x can shield the P-contact deposition, leaving that area unpassivated.

We have found that undercutting can be significantly suppressed by adding sodium dodecylbenzenesulfonate (SDBS, $\text{C}_{18}\text{H}_{25}\text{NaO}_3\text{S}$) to the KOH solution. By varying the concentration of the additive, we could achieve precise control of the etching rate within the range 3–30 nm min⁻¹. Previous studies indicated that incorporating surfactants into the KOH solution can modify both the etch rates and the undercutting^{33,34}. The surfactant molecules create a dense layer on specific crystal orientations and inhibit the chemical reaction between the alkaline solution and silicon atoms. In this work, we speculate that the anionic SDBS additive adsorbs more at the SiN_x interface, where it has positive fixed charges, so that it effectively suppresses lateral chemical reactions, which results in minimal undercutting (Extended Data Fig. 5c,d). A clear correlation between the undercut depth and V_{oc} was observed experimentally, complementing our understanding of the power loss in the back-contact cell process (Extended Data Fig. 5e).

Terawatt-scale sustainability

To achieve carbon neutrality by mid-century, annual PV production is projected to reach 3 TW by 2032³⁵. A sustainability assessment of PV

technologies at the terawatt-scale, thus, has significance. We developed a tailored ESMRC model (efficiency, scalability, manufacturability, reliability and circularity) for this evaluation (Extended Data Table 2). Silicon PV technologies, such as passivated-emitter rear contact (PERC), tunnel oxide passivated contact (TOPCon), SHJ and HBC, demonstrate cell efficiencies surpassing the 25.0% threshold. Moreover, the solar panels are reliable in field applications. These solar panels typically attain over 93% recovery yield of materials, confirming good circularity³⁶. Scalability and manufacturability emerge as decisive factors for terawatt-scale sustainability concerns.

A 25% compound annual growth rate (CAGR) is required to reach 3 TW annual PV production by 2030 (Fig. 4a). Critical material supply, particularly silver and indium, limits the scalability of Si PV technologies, although the supply of Si is sufficient (Extended Data Table 3). Capping annual Ag consumption at 20% of total production severely restricts annual PV production to 637 GW due to the current supply of around 5,200 tonnes yr⁻¹ and a minimum Ag amount per cell of 8 mg W⁻¹ (ref. 37). Meeting the 3 TW production target by 2030 entails a virtually impossible CAGR of 36% or 16% for Ag supply (15 and 5 mg W⁻¹, respectively), even if the price does not surge. Hence, alternative technologies for metallizing Si solar cells using abundant materials, such as copper (Cu), are in urgent need. Indium-based PV technologies, like SHJ and HBC, could sustain 3 TW annual production if each cell has an ITO layer of around 3 nm and assuming 20% consumption of the world indium production per annum. This poses a significant technological challenge for heterojunctions. We achieved 26.5% efficiency with In-less HBC solar cells using a 7 nm ITO layer (Fig. 4b). To address

conductivity needs, we applied 30 nm SnO_2 onto the ultra-thin ITO layer. This positions HBC as a terawatt-scale technology that could satisfy 30% of the total PV demand (a 16% CAGR would meet the full demand). We also demonstrated 26.2% efficiency for HBC solar cells metallized by screen-printed low-temperature Cu paste (Fig. 4c). We expect that, after further advances in these technologies, In-less in combination with Cu-metallized HBC could become an important component technology for reaching the 3 TW target, thereby supporting the transition to renewable energy for carbon neutrality. Overall, in the ESMRC evaluation, HBC outperformed PERC, TOPCon and SHJ in efficiency and scalability but was inferior in terms of manufacturability (Fig. 4d). PERC and TOPCon have scalability limitations because they rely on silver contacts. This is especially evident in TOPCon solar cells, as the extensively used laser-enhanced contact optimization process is applicable only for fired silver contacts³⁸.

The remaining manufacturability concerns, namely extra patterning steps and high capital expenditure, lessen HBC's advantage. Using laser patterning enhanced HBC's performance in the ESMRC evaluation (Fig. 4e). For HBC, the effective process time, defined as the total process time excluding intermediate handling steps, was merely one-third of that for TOPCon (Fig. 4f). Additionally, this low-temperature process has a low carbon footprint. Upscaling a PV technology to large-scale manufacturing usually calls for collective efforts across the industry. We have fabricated a 634 W solar module assembled from 144 pieces of 182 mm \times 91 mm HBC solar cells, with a median efficiency of 26.8% for our pilot production line (Extended Data Fig. 6). We emphasize that HBC is a prominent terawatt-scale technology that could reduce the capital expenditure needed for mass production. Insights from analogous experiences in the electric vehicle manufacturing sector could enrich our understanding of HBC technology. In the near future, exploring a hybrid structure with promising theoretical efficiency could reduce the costly use of parallel-plate plasma-enhanced chemical vapour deposition (PECVD) by one-third to two-thirds³⁹.

Online content

Any methods, additional references, Nature Portfolio reporting summaries, source data, extended data, supplementary information, acknowledgements, peer review information; details of author contributions and competing interests; and statements of data and code availability are available at <https://doi.org/10.1038/s41586-024-08110-8>.

- Ballif, C., Perret-Aebi, L.-E., Lufkin, S. & Rey, E. Integrated thinking for photovoltaics in buildings. *Nat. Energy* **3**, 438–442 (2018).
- Araki, K. et al. *State-of-the-Art and Expected Benefits of PV-Powered Vehicles*. Report No. IEA-PVPS T17-01-2021 (Eindhoven Univ. of Technology, 2021).
- Chu, Y., Ho, C., Lee, Y. & Li, B. Development of a solar-powered unmanned aerial vehicle for extended flight endurance. *Drones* **5**, 44 (2021).
- Schwartz, R. J. & Lammert, M. D. Silicon solar cells for high concentration applications. In *Proc. 1975 International Electron Devices Meeting* (eds Holton, W. C. & Berglund, C. N.) 350–352 (IEEE, 1975).
- King, R. R., Sinton, R. A. & Swanson, R. M. Doped surfaces in onesun, point-contact solar cells. *Appl. Phys. Lett.* **54**, 1460–1462 (1989).
- Lu, M., Bowden, S., Das, U. & Birkmire, R. Interdigitated back contact silicon heterojunction solar cell and the effect of front surface passivation. *Appl. Phys. Lett.* **91**, 063507 (2007).
- Nakamura, J. et al. Development of heterojunction back contact Si solar cells. *IEEE J. Photovolt.* **4**, 1491–1495 (2014).
- Masuko, K. et al. Achievement of more than 25% conversion efficiency with crystalline silicon heterojunction solar cell. *IEEE J. Photovolt.* **4**, 1433–1435 (2014).
- Yoshikawa, K. et al. Silicon heterojunction solar cell with interdigitated back contacts for a photoconversion efficiency over 26%. *Nat. Energy* **2**, 17032 (2017).
- Lin, H. et al. Silicon heterojunction solar cells with up to 26.81% efficiency achieved by electrically optimized nanocrystalline-silicon hole contact layers. *Nat. Energy* **8**, 789–799 (2023).
- Rienäcker, M. et al. Recombination behavior of photolithography-free back junction back contact solar cells with carrier-selective polysilicon on oxide junctions for both polarities. *Energy Procedia* **92**, 412–418 (2016).
- Tomasi, A. et al. Simple processing of back-contacted silicon heterojunction solar cells using selective-area crystalline growth. *Nat. Energy* **2**, 17062 (2017).
- Xu, M. et al. Simple emitter patterning of silicon heterojunction interdigitated back-contact solar cells using damage-free laser ablation. *Sol. Energy Mater. Sol. Cells* **186**, 78–83 (2018).
- Desrues, T., Vecchi, S. D., Souche, F., Muñoz, D. & Ribeyron, P. J. *Slash concept: a novel approach for simplified interdigitated back contact solar cells fabrication*. In *Proc. 38th IEEE Photovoltaic Specialists Conference* (ed. Stanberry, B. J.) 001602–001605 (IEEE, 2012).
- Vasudevan, R. et al. Laser-induced BSF: a new approach to simplify IBC-SHJ solar cell fabrication. *AIP Conf. Proc.* **1999**, 040024 (2018).
- Masuko, K. Method for manufacturing solar cell. International patent WO/2016/152022 (2016).
- Brendel, R. & Peibst, R. Contact selectivity and efficiency in crystalline silicon photovoltaics. *IEEE J. Photovolt.* **6**, 1413–1420 (2016).
- Reichel, C., Granek, F., Hermle, M. & Glunz, S. W. Investigation of electrical shading effects in back-contacted back-junction silicon solar cells using the two-dimensional charge collection probability and the reciprocity theorem. *J. Appl. Phys.* **109**, 024507 (2011).
- Ru, X. et al. 25.11% efficiency silicon heterojunction solar cell with low deposition rate intrinsic amorphous silicon buffer layers. *Sol. Energy Mater. Sol. Cells* **215**, 110643 (2020).
- Li, Y. et al. Flexible silicon solar cells with high power-to-weight ratios. *Nature* **626**, 105–110 (2024).
- Walch, S. P., Ramalingam, S., Sriraman, S., Aydil, E. S. & Maroudas, D. Mechanisms and energetics of SiH_3 adsorption on the pristine $\text{Si}(001)\text{-}(2\times 1)$ surface. *Chem. Phys. Lett.* **344**, 249–255 (2001).
- von Keudell, A. & Abelson, J. R. Direct insertion of SiH_3 radicals into strained Si-Si surface bonds during plasma deposition of hydrogenated amorphous silicon films. *Phys. Rev. B* **59**, 5791–5798 (1999).
- Ramalingam, S., Maroudas, D., Aydil, E. S. & Walch, S. P. Abstraction of hydrogen by SiH_3 from hydrogen-terminated $\text{Si}(001)\text{-}(2\times 1)$ surfaces. *Surf. Sci.* **418**, L8–L13 (1998).
- Copel, M. & Tromp, R. M. H coverage dependence of $\text{Si}(001)$ homoepitaxy. *Phys. Rev. Lett.* **72**, 1236–1239 (1994).
- Jeong, S. & Oshiyama, A. Adsorption and diffusion of Si adatom on hydrogenated Si(100) surfaces. *Phys. Rev. Lett.* **79**, 4425–4428 (1997).
- Jeong, S. & Oshiyama, A. Structural stability and adatom diffusion at steps on hydrogenated Si(100) surfaces. *Phys. Rev. Lett.* **81**, 5366–5369 (1998).
- Ramalingam, S., Maroudas, D. & Aydil, E. S. Atomistic simulation study of the interactions of SiH_3 radicals with silicon surfaces. *J. Appl. Phys.* **86**, 2872–2888 (1999).
- Lin, G. H., Doyle, J. R., He, M. & Gallagher, A. Argon sputtering analysis of the growing surface of hydrogenated amorphous silicon films. *J. Appl. Phys.* **64**, 188–194 (1988).
- Global semiconductor capacity projected to reach record high 30 million wafers per month in 2024. www.semi.org/en/news-media/press-releases/semi-press-releases/global-semiconductor-capacity-projected-to-reach-record-high-30-million-wafers-per-month-in-2024-semi-reports (2024).
- Xu, M. et al. Laser assisted patterning of a-Si:H: detailed investigation of laser damage. *Phys. Status Solidi Rapid Res. Lett.* **11**, 1700125 (2017).
- Harrison, S. et al. Back contact heterojunction solar cells patterned by laser ablation. *Energy Procedia* **92**, 730–737 (2016).
- Chichkov, B. N., Momma, C., Nolte, S., von Alvensleben, F. & Tünnermann, A. Femtosecond, picosecond and nanosecond laser ablation of solids. *Appl. Phys. A* **63**, 109–115 (1996).
- Pal, P., Ashok, A., Haldar, S., Xing, Y. & Sato, K. Anisotropic etching in low-concentration KOH: effects of surfactant concentration. *Micro Nano Lett.* **10**, 224–228 (2015).
- Penta, N. K., Amanapu, H. P., Peethala, B. C. & Babu, S. V. Use of anionic surfactants for selective polishing of silicon dioxide over silicon nitride films using colloidal silica-based slurries. *Appl. Surf. Sci.* **283**, 986–992 (2013).
- Verlinden, P. J. Future challenges for photovoltaic manufacturing at the terawatt level. *J. Renew. Sustain. Energy* **12**, 053505 (2020).
- Deng, R., Chang, N. L., Ouyang, Z. & Chong, C. M. A techno-economic review of silicon photovoltaic module recycling. *Renew. Sustain. Energy Rev.* **109**, 532–550 (2019).
- VDMA. *International Technology Roadmap for Photovoltaic (ITRPV) 2022 Results* 14th edn (VDMA, 2023).
- Fellmeth, T. et al. Laser-enhanced contact optimization on iTOPCon solar cells. *Prog. Photovolt. Res. Appl.* **30**, 1393–1399 (2022).
- Long, W. et al. On the limiting efficiency for silicon heterojunction solar cells. *Sol. Energy Mater. Sol. Cells* **231**, 111291 (2021).
- Taguchi, M. et al. 24.7% record efficiency HIT solar cell on thin silicon wafer. *IEEE J. Photovolt.* **4**, 96–99 (2014).
- Nogay, G. et al. Nanocrystalline silicon carrier collectors for silicon heterojunction solar cells and impact on low-temperature device characteristics. *IEEE J. Photovolt.* **6**, 1654–1662 (2016).
- Zhao, Y. et al. Effects of (i)a-Si:H deposition temperature on high-efficiency silicon heterojunction solar cells. *Prog. Photovolt. Res. Appl.* **31**, 1170–1180 (2023).
- Yu, C. et al. Industrial-scale deposition of nanocrystalline silicon oxide for 26.4%-efficient silicon heterojunction solar cells with copper electrodes. *Nat. Energy* **8**, 1375–1385 (2023).
- Liu, W. et al. Flexible solar cells based on foldable silicon wafers with blunted edges. *Nature* **617**, 717–723 (2023).
- Wang, F. et al. Role of hydrogen plasma pretreatment in improving passivation of the silicon surface for solar cells applications. *ACS Appl. Mater. Interfaces* **6**, 15098–15104 (2014).

Publisher's note Springer Nature remains neutral with regard to jurisdictional claims in published maps and institutional affiliations.

Springer Nature or its licensor (e.g. a society or other partner) holds exclusive rights to this article under a publishing agreement with the author(s) or other rightsholder(s); author self-archiving of the accepted manuscript version of this article is solely governed by the terms of such publishing agreement and applicable law.

© The Author(s), under exclusive licence to Springer Nature Limited 2024

Methods

Solar cell fabrication

Cells were fabricated from M6 size ($166 \times 166 \text{ mm} \pm 0.25$) phosphorus-doped n-type Czochralski monocrystalline Si (100) wafers with a resistivity of $0.8\text{--}10 \Omega \text{ cm}$. The bulk lifetime for an injection of $5 \times 10^{14} \text{ cm}^{-3}$ was over 8 ms as determined by Sinton Instruments BCT400 at the ingot level. Saw damage was removed and the wafers were polished before the cell architecture was fabricated. Cell fabrication involved 12 main steps: (1) N-contact formation: the i:a-Si:H layer is deposited in a silane (SiH_4) flow in PECVD chamber 1 at 13.56 MHz and 240°C . Subsequently, the n:a-Si:H layer is deposited in a mixed SiH_4 and PH_3 flow in chamber 2 at 40.68 MHz and 240°C . (2) Mask deposition: A stack of SiN_x /mask-i:a-Si layers is deposited in sequence in PECVD chamber 3 at 13.56 MHz and 190°C . (3) Laser patterning 1 (P1): A pulsed green picosecond laser (100 kHz and 532 nm) with a spot of $250 \mu\text{m}$ is used to ablate the as-deposited films at a power intensity of 876 mJ cm^{-2} to form patterns. (4) Wet chemical cleaning 1 (WET1): The residuals in the region processed in P1 are removed using an alkali (KOH) and an acid (HF) to expose the c-Si surface for subsequent CVD processes. (5) P-contact formation: The p-i:a-Si:H layer is deposited in a silane flow in PECVD chamber 4 at 13.56 MHz and 190°C . Subsequently, the p:a-Si:H layer is deposited in a mixed SiH_4 and B_2H_6 flow in chamber 5 at 40.68 MHz and 190°C . (6) Laser patterning 2 (P2): A pulsed green picosecond laser (100 kHz and 532 nm) with a spot size of $250 \mu\text{m}$ is used to ablate the designed N-contact regions to remove the overlying P-contact layers. (7) Wet chemical cleaning 2 (WET2): The cell is cleaned ($\text{HCl}/\text{H}_2\text{O}_2$) and dipped in HF for subsequent CVD process. (8) Front passivation: The front i:a-Si:H layer is deposited in PECVD chamber 6 at 13.56 MHz and 240°C , followed by $\text{SiN}_x/\text{SiO}_x$ stack deposition in chamber 7 at 13.56 MHz and 190°C . (The front i:a-Si:H layer is the amorphous silicon layer used to passivate the front surface.) (9) Wet chemical cleaning 3 (WET3): The cell is dipped into HF to remove wrap-around $\text{SiN}_x/\text{SiO}_x$ (the front film was thinned by $10\text{--}15 \text{ nm}$ in step 8). (10) TCO (transparent conductive oxide) deposition: An ITO ($\text{In}_2\text{O}_3:\text{SnO}_4$) layer is deposited using direct current sputtering at 160°C . (11) Laser patterning 3 (P3): A pulsed ultraviolet picosecond laser (400 kHz and 355 nm) is used to ablate the designed gap region to remove the ITO for isolation. (12) Metallization: Silver paste is screen-printed onto the contacts and fired at 170°C in air ventilation to form electrodes. After screen-printing, the Cu paste is fired at the same temperature but in ambient N_2 . After fabrication, high-intensity illuminated annealing is performed under 60 kW m^{-2} and 200°C for 90 s. An LED light matrix (wavelength 400–800 nm) is used for illumination.

Characterization and simulation

The current–voltage ($I\text{--}V$) characteristics of the solar cells were measured using a Sinton FCT-650 IV tester under standard test condition (AM 1.5 G, $1,000 \text{ W m}^{-2}$ and 25°C). The effective lifetime was obtained from a Sinton Instruments WCT-120 instrument in transient mode. The surface recombination parameter J_0 was extracted using the Kane and Swanson method. The contact resistivity was measured using the Cox and Strack method. The current loss induced by electrical shading was characterized by our in-house light-beam-induced current system. Measurements were made by a HORIBA LabRAM Odyssey instrument, with a laser (532 nm, $20 \mu\text{m}$ spot size and 70 mW) as the light-beam source. The platform was moved when scanning. A precision Keithley 2450 source meter was used to measure the induced current.

The thickness, refractive index (n) and extinction coefficient (k) of the single layers were acquired from a J.A. Woollam M-2000 Ellipsometer. The microstructure (R^*) and hydrogen content (C_{H}) of the intrinsic a-Si:H layers were acquired from Fourier transform infrared spectroscopy using a Nicolet IS-10 spectrometer according to the following formulae:

$$R^* = \frac{I_{2,100}}{I_{2,000} + I_{2,100}},$$

$$C_{\text{H}} = \frac{N_{\text{H}}}{N_{\text{H}} + N_{\text{Si}}},$$

$$N_{\text{H}} = A_{2,000} \times I_{2,000} + A_{2,100} \times I_{2,100},$$

where $A_{2,000} = 9.0 \times 10^{19} \text{ cm}^{-2}$ and $A_{2,100} = 2.2 \times 10^{20} \text{ cm}^{-2}$ are proportionality constants for the hydrogen stretching mode at $2,000 \text{ cm}^{-1}$ and $2,100 \text{ cm}^{-1}$. $I_{2,000}$ and $I_{2,100}$ are the integrated absorption peak intensities at $2,000$ and $2,100 \text{ cm}^{-1}$, respectively. N_{H} is the atomic density of hydrogen, and $N_{\text{Si}} = 5 \times 10^{22} \text{ cm}^{-3}$ is the atomic density of pure silicon. The relative reaction rate coefficient K^* is defined as the ratio of reaction rate constant k at temperatures T_2 to T_1 . The Arrhenius equation determines that for a chemical reaction:

$$k = c \exp\left(\frac{-E_{\text{a}}}{k_{\text{B}}T}\right),$$

where c is the frequency factor, E_{a} the activation energy, k_{B} the Boltzmann constant and T the temperature. Accordingly, K^* can be expressed as:

$$K^* = \exp\left(\frac{E_{\text{a}}}{k_{\text{B}}}\left(\frac{1}{T_1} - \frac{1}{T_2}\right)\right).$$

Even without knowing the frequency factor, it is still possible to assess the relative change of the reaction rate from K^* .

When a film was too thin to be measured by the ellipsometer (for example, i_0 , i_1 and i_2), a much thicker version was prepared by extending the deposition time, and this was measured. The thickness of the actual thin layer was then estimated by assuming it was proportional to the deposition time.

The transient thermal response in each layer following laser fluence was simulated using the finite element method in COMSOL Multiphysics 6.1. The simulation couples the two-temperature model with the wave optics module to give a comprehensive analysis of the thermal and optical intricacies inherent in the process. The input parameters for the two-temperature model were sourced from publicly available reports. The optical inputs, specifically the absorption coefficient (α) for the wave optics modelling, were obtained from measurements of individual layers. The absorption coefficient was determined using the Beer–Lambert Law, where $\alpha = 2.303A/t$, with A representing the absorbance and t denoting the thickness of the film. The layer's absorbance was measured using a LAMBDA 1050 + UV/Vis/NIR spectrophotometer.

The $I\text{--}V$ characteristics of the solar cells were simulated in Quokka 3.

The ESMRC model

From a first-principle perspective, the ESMRC model evaluates the sustainability of a PV technology in five dimensions: efficiency, scalability, manufacturability, reliability and circularity. Efficiency pertains to the solar cell's conversion of solar energy to electricity. Scalability examines critical material demands and supply dynamics for widespread deployment. Manufacturability assesses the efficiency of production processes in terms of cost and market competitiveness. Reliability gauges the consistency of the performance of a solar panel under different conditions. Circularity evaluates the technology's alignment with circular economy principles, especially recycling and sustainable resource utilization. Supplementary Table 1 summarizes key aspects of the ESMRC factors, assessed on a scale from very low (1) to very high (5), with the scale representing scores of 1, 2, 3, 4 and 5 for very low, low, medium, high and very high, respectively (Extended Data Table 2).

The scalability assessment concentrates on the critical material demand and supply required to achieve 3 TW of annual PV production by 2030. Silicon solar cells commonly incorporate elements such

as silicon (Si), boron (B), phosphorus (P), oxygen (O), hydrogen (H), nitrogen (N), silver (Ag), aluminium (Al), copper (Cu), indium (In) and tin (Sn). These elements are classified as earth-abundant (Si, B, P, O, H, N, Al, Cu and Sn), rare (In) and noble (Ag). The critical evaluation focuses on Si, In and Ag to determine whether their annual production and supply can meet the demands of the PV industry's expansion. The data used for the assessment were sourced from the United States Geological Survey⁴⁶. Data on annual PV production capacity were obtained from the International Technology Roadmap for Photovoltaics published by the Mechanical Engineering Industry Association⁴⁷. Annual PV production was estimated as the product of the PV production capacity and an optimal utilization rate of 0.85 (Extended Data Table 3).

Data availability

The original data supporting the current study are available from the lead contact on request.

46. *Mineral Commodity Summaries 2023* (USGS, 2023); <https://pubs.usgs.gov/publication/mcs2023>.
47. *International Technology Roadmap for Photovoltaic (ITRPV)* (VDMA, 2023); www.vdma.org/international-technology-roadmap-photovoltaic.

Acknowledgements This work has been supported by the National Natural Science Foundation of China (Grant No. 2022YFB4200100).

Author contributions H.W. and F.Y. contributed equally to this work in designing the HBC solar cell. Miao Yang, Z.H., X.T., Yong Liu, Ping Li, H.C. and M.Q. developed the PECVD process. F.L., J.Z. and T.Y. developed the wet chemical process. Xiyuan Tang, X.D. and S.Z. developed the laser process. Junzhe Wei developed the photolithography process. Q.T., Peng Li, J.C. and B.H. developed the cell metallization. G.W. and H.L. performed the cell simulation. Z.S. performed the laser process simulation. H.Q., Yunpeng Li, L.X., Mingzhe Yu and Q.S. carried out the characterization and data analysis. B.L. and F.P. managed the cell measurements. Y.Y., X.R. and Jianbo Wang developed the cells for the module. Jun Duan assembled the solar module. Q.X., C.L. and S.Y. developed the indium-less TCO layers. C.S., Y.W., H.D. and Tian Xie provided the high-quality wafer. C.X. and X.X. developed the ESMRC model. C.X., H.W., L.X. and C.S. prepared the manuscript. P.G., Q.K., Y.Z., H.Y., N.Y. and Jianning Ding supervised the study. L.C. and J.L. supported the team operation. L.F., Z.L. and X.X. established the research and development plan and led the team in achieving the record efficiency. All authors provided feedback and comments.

Competing interests The authors declare no competing interests.

Additional information

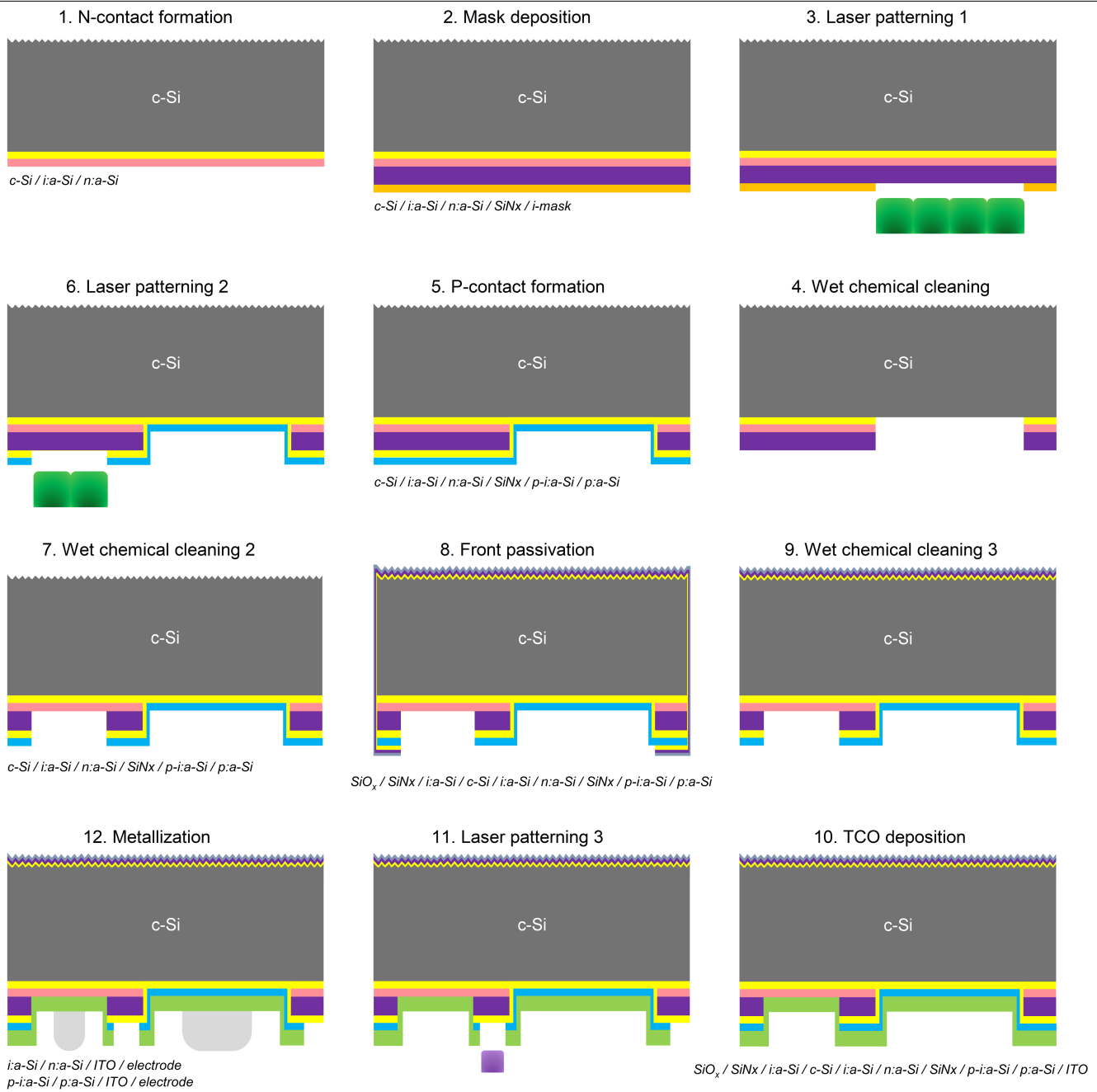
Supplementary information The online version contains supplementary material available at <https://doi.org/10.1038/s41586-024-08110-8>.

Correspondence and requests for materials should be addressed to Chaowei Xue, Jianning Ding, Liang Fang, Zhenguo Li or Xiang Xu.

Peer review information *Nature* thanks Xinbo Yang and the other, anonymous, reviewer(s) for their contribution to the peer review of this work. Peer reviewer reports are available.

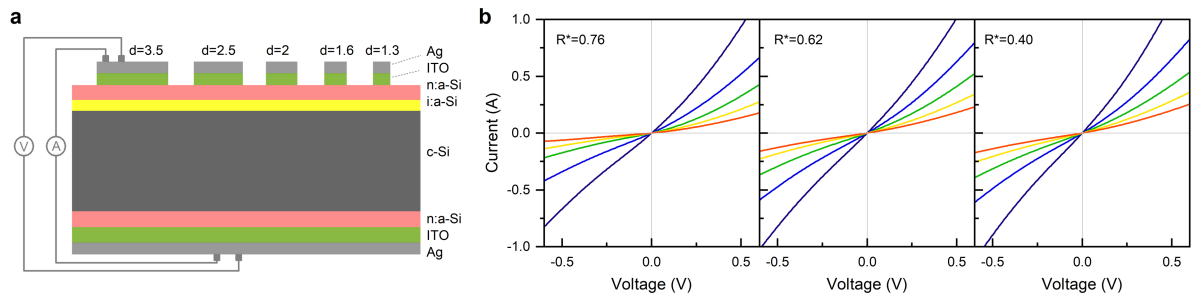
Reprints and permissions information is available at <http://www.nature.com/reprints>.

Article

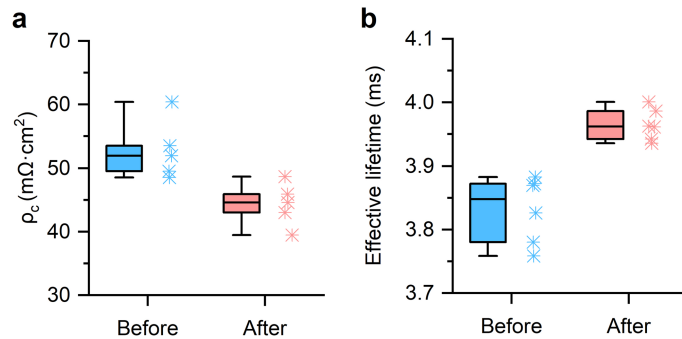


Extended Data Fig. 1 | A complete fabrication process flow of the HBC solar cell. The cell fabrication process comprises 12 major steps including **1. N-contact formation**, **2. Mask deposition**, **3. Laser patterning 1**, **4. Wet chemical cleaning**, **5.**

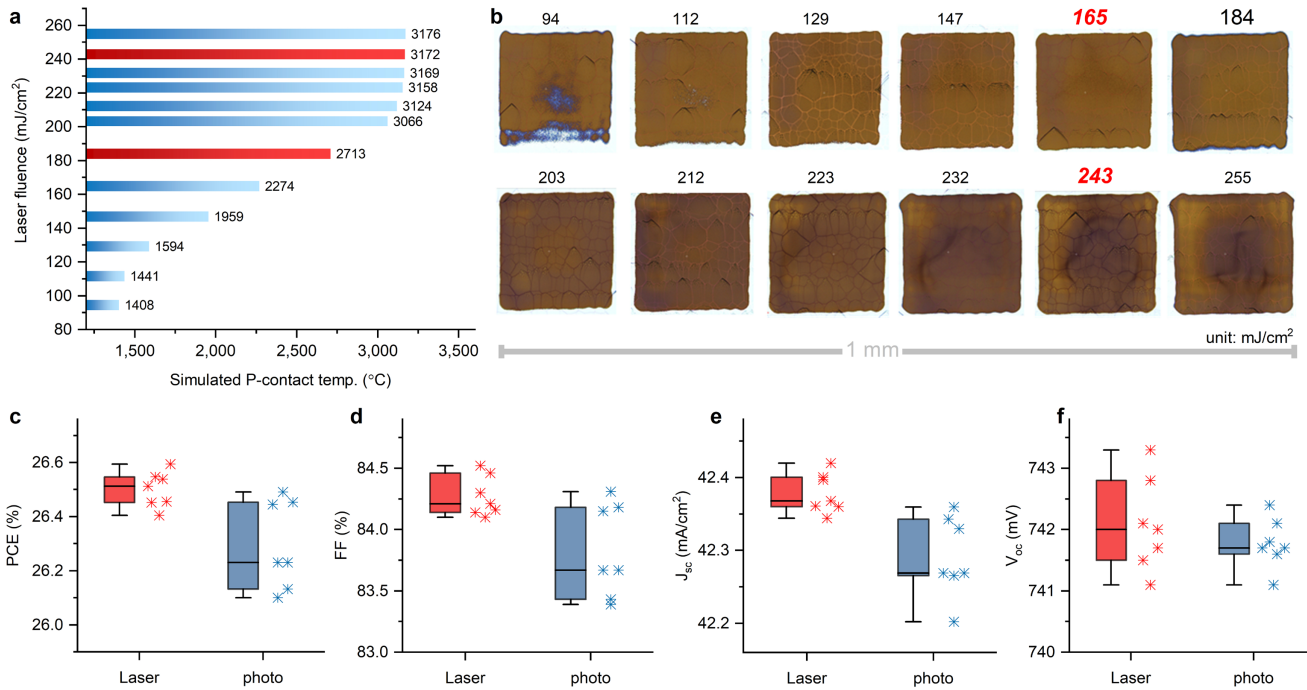
P-contact formation, **6. Laser patterning 2**, **7. Wet chemical cleaning 2**, **8. Front passivation**, **9. Wet chemical cleaning 3**, **10. TCO deposition**, **11. Laser patterning 3**, and **12. Metallization**.



Extended Data Fig. 2 | Contact resistivity measurement. **a.** Diagram depicting sample configuration for the measurement. The diameters of the disks are in millimetre. **b.** Current-voltage curves obtained for samples with different R^* values.

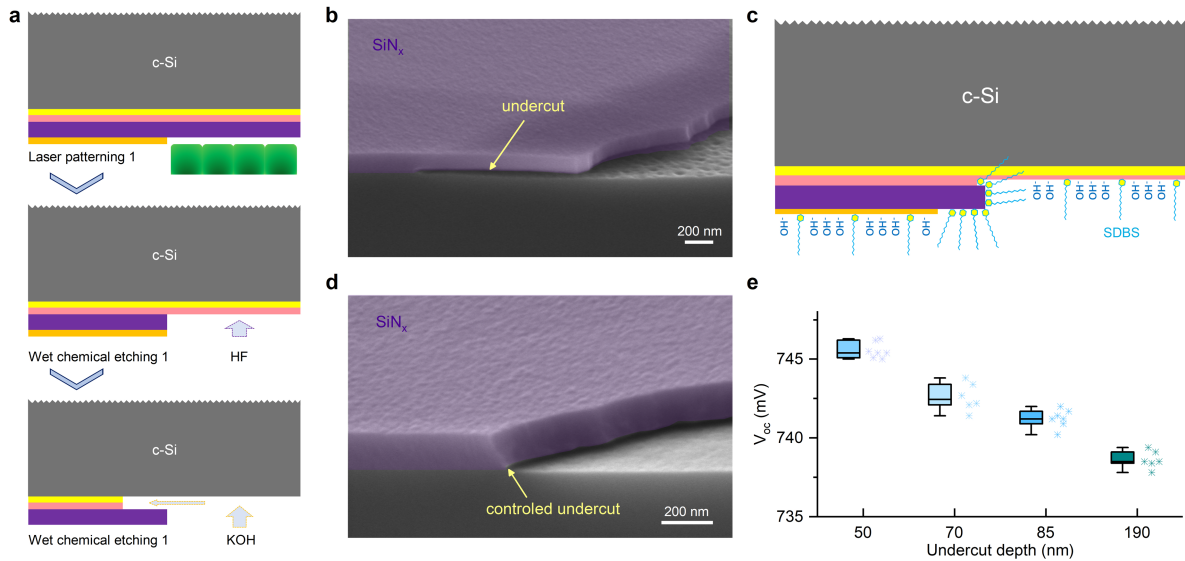


Extended Data Fig. 3 | Effect of high-intensity illuminated annealing on N-contact. **a**, Vertical contact resistivity of i/n/ITO/Ag. **b**, Effective lifetime at $\Delta n = 5 \times 10^{15}$ cm 3 measured on samples symmetrically passivated by i-a-Si:H/n-a-Si:H, before and after high-intensity illuminated annealing. The top lines, bottom lines, lines in the box, and boxes represent maximum values, minimum values, median values, and 25–75% distributions, respectively.



Extended Data Fig. 4 | The evolution of P-contact temperature and resulting features in laser spots at various laser fluence in P2 patterning, and IV performance of solar cells fabricated via all laser patterning processes compared to photolithography processes. **a.** Simulated P-contact temperature at increasing laser fluence. **b.** Features post-laser spallation at increasing energy deposition observed under an optical microscope. The bold red numbers 184 and 243 mark correspond to the first and second inflection

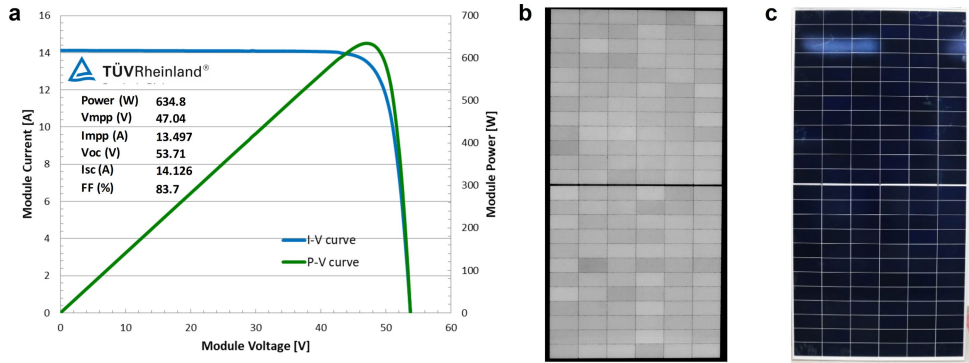
points in Fig. 3c. **c to f**, solar cells' PCE, FF, J_{sc} and V_{oc} are plotted using grouped box charts, with median value lines displayed in each group. The “Laser” group shows devices using complete laser patterning, and those in the “photolithography (photo)” group use photolithography for P3 but the same laser processes for P1 and P2. In **c-f**, the top lines, bottom lines, lines in the box, and boxes represent maximum values, minimum values, median values, and 25–75% distributions, respectively.



Extended Data Fig. 5 | The formation of undercut and its influence on solar cell's V_{oc} . **a.** Illustration of the P1 and WET process for undercut formation.

b. Scanning electron microscopy (SEM) image showing the undercut between SiN_x layer and the c-Si substrate. **c.** Schematic of SDBS additive controlling undercut. **d.** SEM image showing controlled undercut. **e.** The relationship

between undercut depth and V_{oc} , obtained by four groups of solar cells by varying alkaline etching conditions. Cross-section SEM images of 6 samples in each group were taken to assess the undercut depth (median values). The top lines, bottom lines, lines in the box, and boxes represent maximum values, minimum values, median values, and 25–75% distributions, respectively.



Extended Data Fig. 6 | The HBC solar module performance. **a.** The IV and PV curves of HBC module (testing laboratory: TÜV Rheinland (Suzhou) Co.,Ltd.).

b. Electron luminescence (EL) image of the tested module. **c.** Front view of the

tested module. The module is assembled of 144 pieces of 182 mm×91 mm cells with a median efficiency of 26.8%.

Article

Extended Data Table 1 | Process parameters for deposition of component layers

a

Approach	Component	Temperature	Pressure	Power density	SiH ₄ flow	H ₂ flow	Thickness	R*
	Layer	(°C)	(mtorr)	(mW/cm ²)	(sccm)	(sccm)	(nm)	(%)
Porous i0	i0	170-200	900-1300	50-100	1100-1600		1.2	50-70
	i1	170-200	500-1000	50-100	1100-1600		2.1	50-60
	i2	170-200	500-1000	50-100	200-800	2000-4000	3.4	10-30
SPET	i0	210-250	500-800	100-300	500-800		1.2	30-50
	i1	210-250	500-800	50-100	500-800		2.1	20-40
	i2	210-250	900-1300	50-100	100-400	1500-3000	3.4	10-20

b

Component	Temperature	Pressure	Power density	SiH ₄	H ₂	PH ₃	B ₂ H ₆	NH ₃	CO ₂
Layer	(°C)	(mtorr)	(mW/cm ²)	(sccm)	(sccm)	(sccm)	(sccm)	(sccm)	(sccm)
n:a-Si:H	200-250	500-800	50-100	100-300	400-1200	300-900			
p:a-Si:H	180-200	700-1000	50-100	100-300	300-900		50-150		
SiN _x	170-200	900-1300	100-150	100-200	5000-8000			500-1000	
SiO _x	170-200	500-800	100-150	100-200	1000-3000				300-800

c

Component	Temperature	Pressure	O ₂ / Ar	Power density	Power supply	SnO ₂ wt.
layer	(°C)	(Pa)	flow ratio	(kW/m ²)	type	(%)
ITO	150-200	0.3~0.5	0.05-0.10	2.8-4.0	DC	10
SnO ₂	25 (RT)	0.3~0.5	0.10-0.20	2.8-4.0	DC	100

a. PECVD process parameters for the deposition of the i0/i1/i2 stack. b. PECVD process parameters for the deposition of the n:a-Si:H, and p:a-Si:H contacts, and the SiN_x and SiO_x layers. c. PVD process parameters for the deposition of ITO and SnO₂ layers.

Extended Data Table 2 | ESMRC evaluation of major Si PV technologies

ESMRC factor	Aspect	PERC		TOPCon		SHJ		HBC	
		Detail	Score	Detail	Score	Detail	Score	Detail	Score
Efficiency	Record PCE	25.0%	3	26.1%	4	26.8%	4.5	27.3%	5
Scalability	Critical material	Ag	4	Ag	4	Ag, In	3	Ag, In	5
Manufacturability	Production complexity	9 steps	5	12 steps	4.5	6 steps	4.5	15 steps	4
	CAPEX	Tube furnace, ALD		Tube furnace, LPCVD, ALD		Parallel-plate PECVD, PVD		Parallel-plate PECVD, PVD	
	Environmental impact	Nontoxic, WET x2		Nontoxic, WET x3		Nontoxic, WET x1		Nontoxic, WET x3	
Reliability	Long-term stability	25 years	5	25 years	5	25 years	5	25 years	5
Circularity	Recyclability	>93%	4	>93%	4	>93%	4	>93%	4

Article

Extended Data Table 3 | Calculation of critical material demand to sustain 3 TW/year PV production

Si demand									
Si density	Cell Area ¹	Cell Thickness ²	Si consumption	PCE	Power	Si consumption	PV Capacity ⁴	Si demand	CAGR
g/cm ³	cm ²	um	g/cell	%	W	g/W	TW/year	1000 ton	%
2.33	220.5	120	6.17	23	5.07	1.216	3	3647	2
2.33	220.5	120	6.17	25	5.51	1.118	3	3355	1
2.33	220.5	120	6.17	26 ³	5.73	1.075	3	3226	N/A ⁵
2.33	220.5	120	6.17	27	5.95	1.036	3	3107	N/A
In demand, In₂O₃:SnO₂ (90:10)⁶									
In density	Cell area	ITO thickness	In consumption	PCE	Power	In consumption	PV capacity	In demand	CAGR
g/cm ³	cm ²	nm	mg/cell	%	W	mg/W	TW/year	ton	%
7.13	220.5	30	4.72	27	5.95	0.79	3	2377	43
7.13	220.5	20	3.14	27	5.95	0.53	3	1584	35
7.13	220.5	10	1.57	27	5.95	0.26	3	792	22
7.13	220.5	7	1.10	27	5.95	0.18	3	555	16
Ag demand				¹ Half-cell area based on 210 x 210 mm size					
Ag Consumption ⁷	PV capacity	Ag demand	CAGR	² ITRPV expected solar cell thickness by 2030					
mton/GW	TW/year	mton	%	³ TOPCon, SHJ and HBC seeing mass-production in 26% PCE					
5	3	15000	16	⁴ Assuming 100% cell to module power ratio					
10	3	30000	28	⁵ N/A means that the demand can be met with the current supply					
15	3	45000	36	⁶ ITO raw material (atomic ratio): 90 % In ₂ O ₃ and 10% SnO ₂					
				⁷ ITRPV expected Ag consumption by 2030					